5
Solution-Processable Benzothiazole-Substituted Formazanate Zinc(II) Complex Designed for Robust Resistive Memory Device

Research Article based on this study:

Birara, S., Saini, S., Majumder, M., Lama, P., Tiwari, S. P., & Metre, R. K. (2024). Solution-Processable Benzothiazole-Substituted Formazanate Zinc(II) Complex Designed for Robust Resistive Memory Device. Dalton Transactions, 53 (36), 15338-15349.

5.1 Introduction

With information data growing at an exponential rate, there has been a critical demand for developing new memory devices with high performance [Y. Li et al., 2020; Lian et al., 2022b; Shao et al., 2019b]. Resistive memory devices have significant potential for achieving high-density data storage within a compact device footprint [Han et al., 2013; Heremans et al., 2011b; W. P. Lin et al., 2014a]. A memristor, or resistive memory, functions as an electrical switch that transitions between high and low conductivity states, and notably, it retains the present resistance even after the electric power source is off. Nevertheless, traditional semiconductor devices made of silicon are currently facing significant limitations in terms of data accuracy, thermal issues, high production costs for large-scale implementation, and a lack of inherent adaptability to flexible deformation due to their predominantly brittle electronic components [Gao et al., 2019]. Thus, there has been a significant global endeavor within academic and industrial communities to advance the development of novel memory materials with exceptional features [Scott & Bozano, 2007]. Numerous materials have been extensively investigated as active components of resistive memory devices, including polymers [Bandyopadhyay et al., 2011a; Hu et al., 2014; W. P. Lin et al., 2014b], two-dimensional materials [Sangwan et al., 2015; Yoshida et al., 2015], inorganic oxides [K. M. Kim et al., 2016; M. J. Lee et al., 2011; Wedig et al., 2016], and diverse molecular systems [Cho et al., 2011; Miao, Li, Xu, Li, Ji, et al., 2012; Miao, Li, Xu, Li, Zheng, et al., 2012; Paul et al., 2012c]. Oxide devices have emerged as the most appealing options in terms of their prospective applications; however, the issues of large set/reset voltage and high forming voltage/current still need to be addressed in order to achieve high-density memories [Gilbert et al., 2013].

Among the other materials, organometallic and transition metal complexes possess advantageous properties for optoelectronic applications due to the intricate structure-property relationships of metal centers and ligands [Chan et al., 2017b; S. J. Liu et al., 2011; Paul et al., 2012b; Seo et al., 2008b; Stoliar et al., 2015b; Xia et al., 2019]. These properties include a diverse range of charge-transfer states, electron-accepting capabilities, remarkable stability, and extensive redox capabilities, which enhance their efficacy in resistance-switching applications. Furthermore, due to their molecular design, these materials have intrinsic benefits such as solution processability and film-forming property, which provides low-cost solution processing for a variety of integrated devices [Shao et al., 2019b]. Numerous comprehensive investigations have been undertaken so far regarding the design, synthesis, and utilization of metal complexes-

based materials and technologies for information storage purposes. Some of the profound works in this area include the use of gold(III) complexes as an active layer for the solution-processable construction of resistive memory devices [Au et al., 2015; Hong et al., 2016c]. Goswami et al. have shown that combined molecular redox processes in conjugation with counterion displacement can produce a switching between two resistive states in ruthenium-coordinated azo aromatics, which in turn produces the resistive memory effect [Goswami et al., 2017b]. Additionally, there have been studies demonstrating the development of non-volatile memory devices using thin films of copper polyphthalocyanine (CuPPc) grown by chemical vapor deposition [Guo et al., 2019]. Bandyopadhyay et al. conducted a study demonstrating non-volatile resistive state switching in a conjugated Co(III) polymer [Bandyopadhyay et al., 2011b]. Kandasamy et al. constructed a range of RRAM devices using polypyridyl Cr(III) complexes and concluded that modifying the ligand design resulted in variations in the coordination sphere, which in turn led to differences in the ON/OFF ratio of the devices, ranging from 10^4 to 10^6 [Kandasamy et al., 2018c]. Our research group has recently demonstrated the behavior of a phenalenyl-based Co(II) complex in a resistive memory device [Kamboj, Betal, et al., 2023].

Traditional inorganic metal oxides are highly desirable as their memory devices offer very good resistive switching properties. Compared to earlier reports involving metal oxides, the current memory material utilizes a transition metal complex that leverages the distinctive properties of formazan ligands. Formazanate metal complexes offer significant advantages over these materials, including high solubility, simple device structures, ease of processing, low fabrication costs, and remarkable versatility [Gilroy & Otten, 2020c]. The approach to designing these resistive memory materials involves creating distinct electronic states under the influence of an electric field. This can be accomplished by adjusting the electron-donating and electron-accepting properties, as well as the charge-transport characteristics of these complexes. Formazanate metal complexes frequently feature highly reversible and easily accessible redox couples, making them ideal candidates for electronic applications. By making modifications to the delocalized formazan-derived ligands and their metal complexes, the optoelectronic properties can be fine-tuned, enabling the synthesis of new materials for information storage. The coordination chemistry of formazanate ligands was first reported in 1941; however, its investigation has had a resurgence in the last decade, mostly driven by the exploration of its electrochemical and optical characteristics [Barbon et al., 2014b; Hunter & Roberts, 1941]. Complexes containing a coordinated formazanate ligand typically exhibit a narrow HOMO–LUMO gap. Thus, the presence of energetically accessible π^*-orbitals in formazanate complexes enables their redox activity, facilitating the reversible ligand-based storage of electrons in these compounds. Zinc complexes of formazanates have also been reported to be able to store up to two electrons within a single formazanate ligand, thereby enabling the development of ligand-based multi-electron chemical transformations [Chang et al., 2015c]. The field of application that has gained significant recognition is mainly based on the optoelectronic characteristics shown by boron difluoride adducts of the formazanate anion [Barbon et al., 2015; Buguis et al., 2022a; C. Kumar et al., 2020; Maar et al., 2015a]. The excellent stability of formazanate boron compounds makes them promising candidates for applications in materials, which is mainly due to the inclusion of redox-active formazanate units in polymers, resulting in a narrow band-gap, which can be further modified through partial reduction. Furthermore, in addition to utilizing the distinctive optoelectronic characteristics associated with formazanate ligands, recent studies have shown that their redox-active capabilities may be used to achieve new catalytic reactivity [de Vries & Otten, 2022]. The comprehensive understanding that has been acquired in the past two decades regarding the synthesis, characteristics, and reactivity of formazanate coordination complexes establishes a strong foundation for the exploration of novel applications that leverage the unique optoelectronic properties and versatile electrochemistry offered by formazanate ligands [Gilroy & Otten, 2020d]. A recent publication by our research group presents a study on an ionic organotin complex that incorporates a 1,5-diphenyl-3-(2-pyridyl)formazan ligand that was used in the designing of a WORM-type memory device [Birara, Betal, et al., 2023b].

Additionally, we investigated the use of a bis(formazanate) Zn(II) complex in resistive-switching random access memory that demonstrated the ability to undergo multilayer switching. In light of our profound interest in metal complexes, including redox-active formazanate ligands and their use in resistive memory devices, we undertook the synthesis and characterization of the bis(formazanate) zinc complex, [$Zn^{II}L1_2$] (**3**) based on formazan based ligand, 1-(benzothiazol-2-yl)-5-(2-benzoyl-4-chlorophenyl)-3-phenylformazan (L1H), in order to investigate its application in non-volatile memory devices. The selection of a Zn^{2+} complex was primarily based on its importance in memory device applications [Birara, Saini, et al., 2023; Q. U. Khan et al., 2017], as well as the intrinsic stability of the Zn^{2+} ion and its ability to maintain a consistent +2 oxidation state when combined with formazanate ligands. In addition, the Zn serves as a dopant, which decreases the HOMO-LUMO gap and increases the electron delocalization within the formazanate backbone. This study also highlights the importance of the N-aryl substituents of the formazanate backbone in influencing the optical and electrochemical properties of the metal complex. The addition of a benzothiazole substituent to the formazanate backbone has resulted in a decrease in the HOMO-LUMO gap in complex **3**. This decrease has improved the donor-acceptor interaction in complex **3**, leading to a higher switching memory performance compared to our previously described bis(formazanate) zinc complex (abbreviated as $Zn^{II}L_2$ (**2**)) in the previous chapter based on 3-cyano-1,5-(4-antipyrinyl)formazan (LH) ligand [Birara, Saini, et al., 2023].

5.2 Experimental Section

5.2.1 General Considerations

All the solvents and chemicals used for the preparation of L1H and **3** were purchased commercially, maintained at room temperature, and used as received without any further purification. In Chapter 2, detailed descriptions of the instruments used for various characterizations are provided.

5.2.2 Synthesis of 1-(benzothiazol-2-yl)-5-(2-benzoyl-4-chlorophenyl)-3-phenylformazan, L1H.

A suspension of 2-hydrazinobenzothiazole (0.330 g, 2.0 mmol, 1.0 eq) in MeOH (25 mL) was treated with glacial acetic acid (0.2 mL), resulting in partial dissolution. After adding benzaldehyde (0.2 mL, 2 mmol, 1.0 eq) in one portion, white precipitates were formed after 5-10 min. In a separate flask, 2-Amino-5-chlorobenzophenone (0.464 g, 2.0 mmol, 1.0 eq) was dissolved in a solution of 12 M HCl (2.0 mL, 24 mmol) in H_2O (20 mL) at 0 ^oC, to which a solution of $NaNO_2$ (0.50 g, 7.3 mmol) in H_2O (5 mL) at 0 ^oC was added resulting in the formation of the corresponding diazonium salt. The mixture was allowed to stir for another 30 minutes, which was further added to the initial reaction mixture dropwise in the presence of NaOH, resulting in the formation of a dark red solid. Further, the coupling reaction mixture was allowed to stir for another 5 h. The red precipitate was collected by filtration and dried overnight. The crude solid was further purified by column chromatography (dichloromethane, neutral alumina) to afford the red solid. Yield: 528 mg (45%). ^1H NMR (500 MHz, $CDCl_3$) δ 12.00 (s, 1H), 8.16 (d, *J* = 8.8 Hz, 1H), 7.98 (d, *J* = 7.8 Hz, 1H), 7.89 – 7.84 (m, 2H), 7.81 (d, *J* = 7.6 Hz, 2H), 7.68 (dd, *J* = 27.2, 7.8 Hz, 2H), 7.63 – 7.48 (m, 4H), 7.46 (dd, *J* = 13.4, 5.6 Hz, 5H), 7.37 – 7.33 (m, 1H) ppm. ^{13}C NMR (126 MHz, $CDCl_3$) δ 195.86, 171.07, 152.67, 146.80, 144.82, 137.13, 134.19, 133.27, 132.45, 130.81, 129.79, 128.97, 128.76, 128.59, 128.45, 127.11, 127.01, 126.44, 125.24, 122.87, 121.72, 121.13 ppm. FT-IR (KBr): 3445 (m), 3055 (m), 1668 (s), 1593 (m), 1539 (s), 1481 (s), 1446 (s), 1317 (m), 1265 (s), 1162 (s), 1118 (m), 1046 (m), 1018 (m), 946 (m), 829 (m), 752 (s), 692 (s) cm^{-1}. UV–vis ($CHCl_3$): λ_{max} 337 nm (ε = 13,800 M^{-1} cm^{-1}), 509 nm (ε = 11,000 M^{-1} cm^{-1}). MS (HRMS, positive-ion mode). Exact mass calcd for $[C_{27}H_{18}ClN_5OS+H]^+$: 496.0921. The exact mass found: 496.1341.

5.2.3 Synthesis of Bis-(1-(benzothiazol-2-yl)-5-(2-benzoyl-4-chlorophenyl)-3 -phenylformazan)Zinc complex, 3.

After dissolving L1H (99.20 mg, 0.2 mmol) in 20 mL of methanol, $Zn(OCOCH_3).2H_2O$ (21.9 mg, 0.1 mmol) was added, and the mixture was stirred for 24 hours at room temperature under nitrogen atmosphere. During this time, the dark blue precipitate formed, which was subsequently isolated and subjected to successive washes using methanol and hexane. Crystals appropriate for X-ray diffraction investigation were acquired using the process of vapor diffusion, wherein hexane was diffused into a concentrated DCM solution of **3**. Yield: 80 mg (70%). ^{1}H NMR (500 MHz, $CDCl_3$) δ 8.22 (d, J = 7.3 Hz, 4H), 7.62 – 7.48 (m, 8H), 7.25 (ddd, J = 22.1, 15.3, 5.2 Hz, 11H), 7.14 (dd, J = 8.6, 1.4 Hz, 2H), 7.05 (dt, J = 15.7, 7.3 Hz, 4H), 6.85 (dd, J = 18.1, 8.0 Hz, 5H) ppm.^{13}C NMR (126 MHz, $CDCl_3$): δ 193.91, 180.14, 147.91, 147.71, 146.25, 135.92, 135.65, 133.93, 132.75, 131.74, 131.50, 130.69, 129.68, 129.37, 128.91, 128.58, 128.30, 128.05, 127.94, 127.47, 123.27, 121.85, 118.10 ppm. FT-IR (KBr): 1664 (m), 1551 (w), 1403 (m), 1227 (m), 1146 (m), 1087 (m), 1055 (m). UV–vis ($CHCl_3$): λ_{max} 326 nm (ε = 7200 M^{-1} cm^{-1}), 651 nm (ε = 10,900 M^{-1} cm^{-1}). Exact mass calcd for $[C_{54}H_{34}Cl_2N_{10}O_2S_2Zn+H]^+$: 1053.1048 Exact mass found: 1053.1108. Anal. Calcd. (%) for $C_{54}H_{34}Cl_2N_{10}O_2S_2Zn$: C, 61.46; H, 3.25; N, 13.27. Found: C, 61.72; H, 3.31; N, 12.89.

5.2.4 Computational Details

ORCA 5.0.2 programs [Neese et al., 2020] were used for the DFT and TD-DFT computations. The geometry of $[Zn^{II}L1_2]$ was optimized by using a GGA functional BP86 method, along with Grimme's dispersion correction, D3BJ,[Allouche, 2012; Grimme et al., 2010] in conjugation with a basis set def2-TZVP49 [Weigend & Ahlrichs, 2005a] on ligands (C, H, N) and an effective core potential (SDD) [Dolg et al., 1986] on the metal atom (Zn). To improve the computational speed, the RI approximation [Kollmar et al., 2019] with a combination of an auxiliary basis set (def2/J)[Weigend, 2006] was also used in all DFT calculations. Frequency analysis were done to confirm the minimum character of all optimized structures (no imaginary frequency). No symmetry restrictions (i.e., C1) were held during the geometry optimizations. The resultant geometries from optimization were used in subsequent single-point energy calculations at the BP86+D3BJ/def2-TZVPP+SDD level of theory. The Natural Bond Order (NBO) analysis was performed at the same level of theory (BP86+D3BJ/def2-TZVPP+SDD//BP86/def2-TZVP+SDD). Avogadro software [Lopez, 2014]was employed to visualize molecular orbitals. The NBO 7.0 program interfaced with ORCA 5.0.2 program was employed for the analysis.

5.2.5 Fabrication of RRAM Device

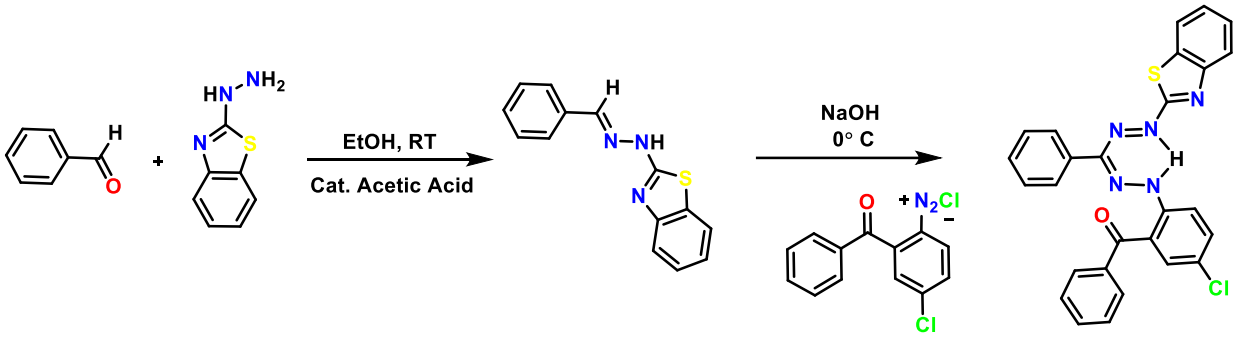
FTO-coated glass substrates were used to fabricate the RRAM device where FTO was considered as BE. Firstly, the cleaning process of FTO-coated glass was done by ultrasonication in isopropyl alcohol (IPA) for 30 minutes and drying with N_2. A 15 mg/ml solution of $[Zn^{II}L1_2]$ (**3**) was prepared in chloroform by stirring for two hours. This solution was spin-coated over BE at 2000 rpm for 45 seconds and annealed at 90℃ for 1 hour. The film thickness of complex **3** was measured to be ~60 nm. Finally, circular shape TEs of 250 μm diameter were deposited using a thermal evaporation machine. The electrical characterization of the fabricated $Ag/[Zn^{II}L1_2]/FTO$ RRAM device was measured with Keithley 4200 SCS.

5.3 Results and Discussion

5.3.1 Synthetic Aspects

Formazan ligand L1H was synthesized by condensing 2-hydrazinobenzothiazole with benzaldehyde, resulting in desired hydrazones. Coupling of in situ generated hydrazone with aryl diazonium chloride salt of 5-chloro-2-benzoylbenzenamine in the presence of NaOH produced a reaction mixture from which it was possible to isolate the desired formazan in moderate yield (Scheme 5.1). This modular synthetic procedure allows the preamble of several different substitution patterns comprising various asymmetric derivatives. Formazan derivative

L1H exhibits straightforward ^{1}H and ^{13}C NMR spectroscopic features, revealing diagnostic formazan NH shifts in the ^{1}H NMR spectra at 12 ppm and consistent with equivalent aromatic groups in both ^{1}H and ^{13}C NMR spectra (Figure 5.1-5.2). Further characterizations of the ligands were carried out using UV-Vis, FT-IR spectroscopy, and mass spectrometry. The identification of N–H weak bands in the FTIR spectral data at the wavelength of 3444 cm^{-1} for L1H suggests the presence of existing intramolecular hydrogen bonding within the formazan molecule (Figure 5.3 (b)). The presence of strong bands at 1481 cm^{-1} for L1H indicates the presence of the –N=N– group. Additionally, the distinct C=N stretching band in formazan is observed at 1593 cm^{-1} for L1H, which aligns well with the published FTIR values [Turkoglu & Berber, 2016]. HRMS studies of L1H showed the presence of the molecular ion peak at 495.0921 (Figure 5.3 (a)).



Scheme 5.1. Synthesis of benzothiazole-substituted formazan, L1H.

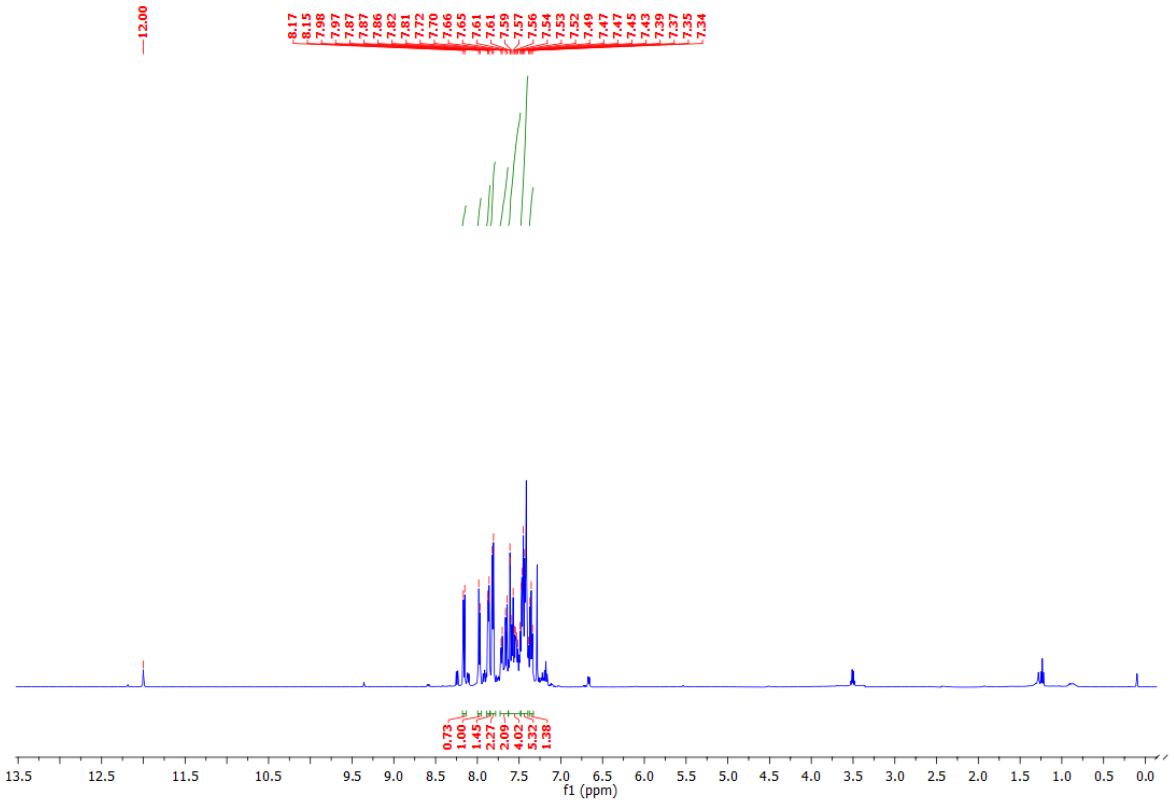


Figure 5.1. ^{1}H NMR of L1H in $CDCl_3$.

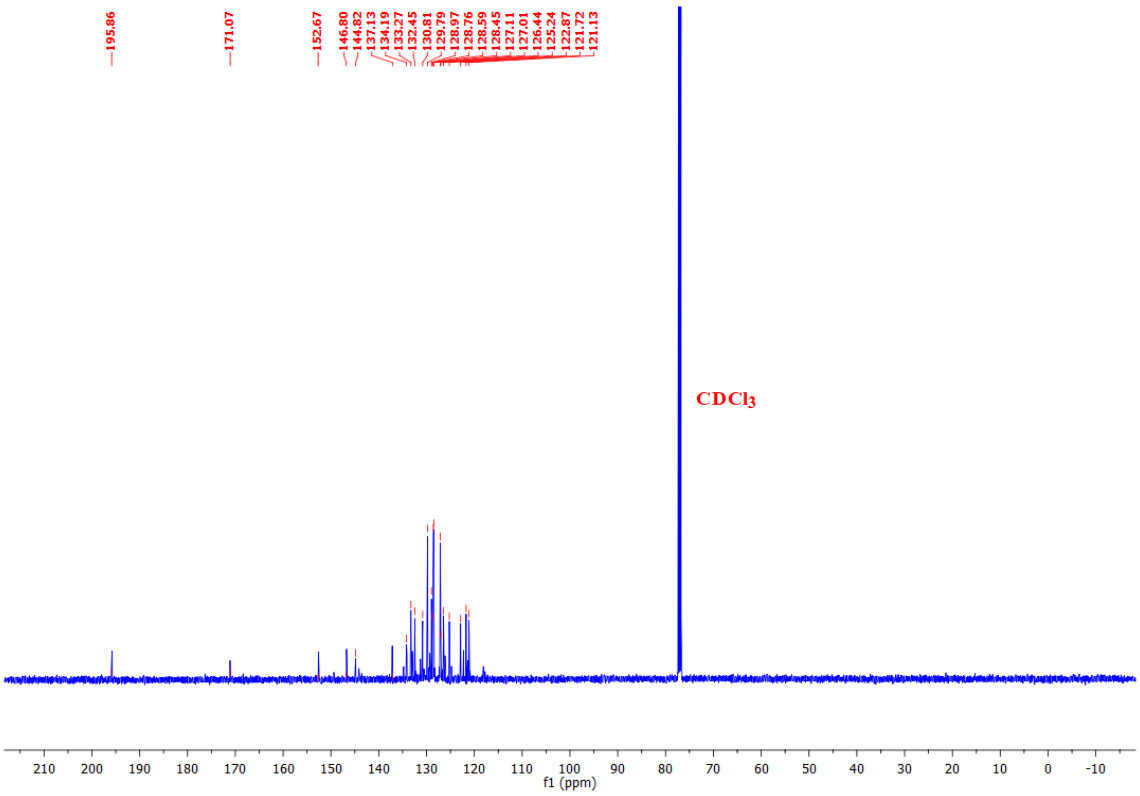


Figure 5.2. $^{13}C\{^{1}H\}$ NMR of L1H in $CDCl_3$.

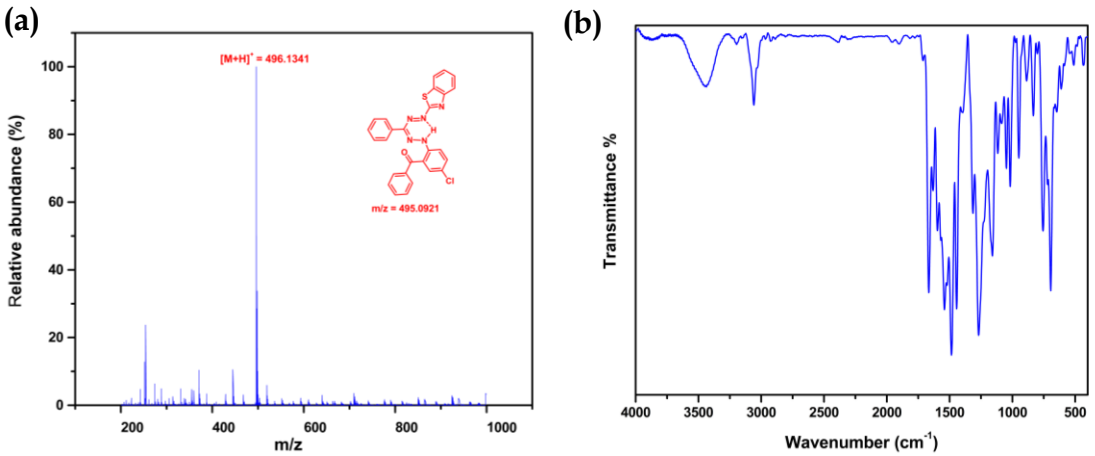
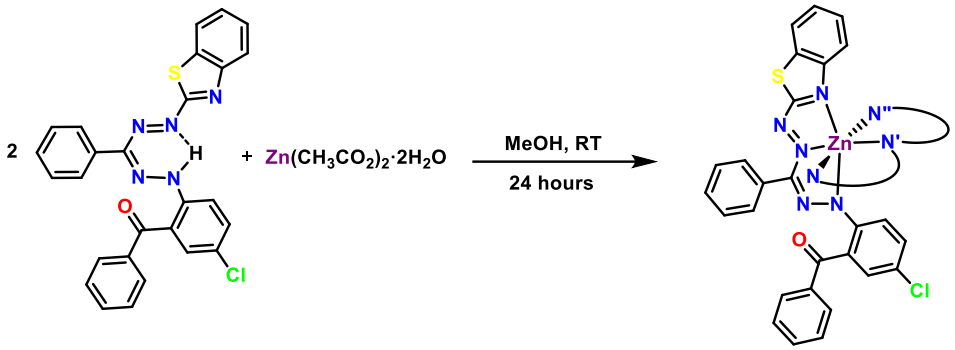


Figure 5.3. (a) HRMS analysis for L1H: Anal. Calcd. for [M+H]+ peak, m/z = 496.0921. Found [M+H]+ peak, m/z = 496.1341 (b) FT-IR spectrum of L1H.

The bis(formazanate) zinc complex (**3**) was synthesized by the reaction of two equivalents of the formazan ligand L1H with one equivalent of zinc acetate dihydrate in a methanolic solution for a duration of 24 hours (Scheme 5.2). The formation of **3** was seen by a visual change in color, namely from red to blue, which was accompanied by the formation of the solid precipitate. This observation was further supported by the absence of the NH resonance of the formazan ligand L1H in the corresponding ^{1}H NMR spectra of the **3** (Figure 5.5). Complex **3** was obtained in a purified yield of 70%, and its characterization was conducted by several analytical techniques, including ^{1}H and $^{13}C\{^{1}H\}$ NMR spectroscopy, UV−vis absorption spectroscopy, FT-IR spectroscopy, cyclic voltammetry, and mass spectrometry. Complex **3** exhibits air stability under ambient conditions. The absence of an N–H weak band in the FTIR spectrum data at the wavelengths of 3444 cm^{-1} for **3** suggests that the ligand binds to the metal in its negatively charged form (Figure 5.4). The bulk purity of **3** was confirmed using elemental analysis (Figure 5.7).

Thermogravimetric analysis (TGA) was used to verify the thermal stability of complex **3**, which was shown to remain stable up to a temperature of 240°C (Figure 5.4 (c)). The complex has a high degree of thermal stability, hence enabling it to withstand heat-induced degradation in the memory device. The HRMS analysis of **3** revealed the presence of a molecular ion peak at m/z 1053.1108 (Figure 5.4 (a)).



Scheme 5.2. Synthesis of bis(formazanate) zinc complex, $[Zn^{II}L1_2]$(**3**)

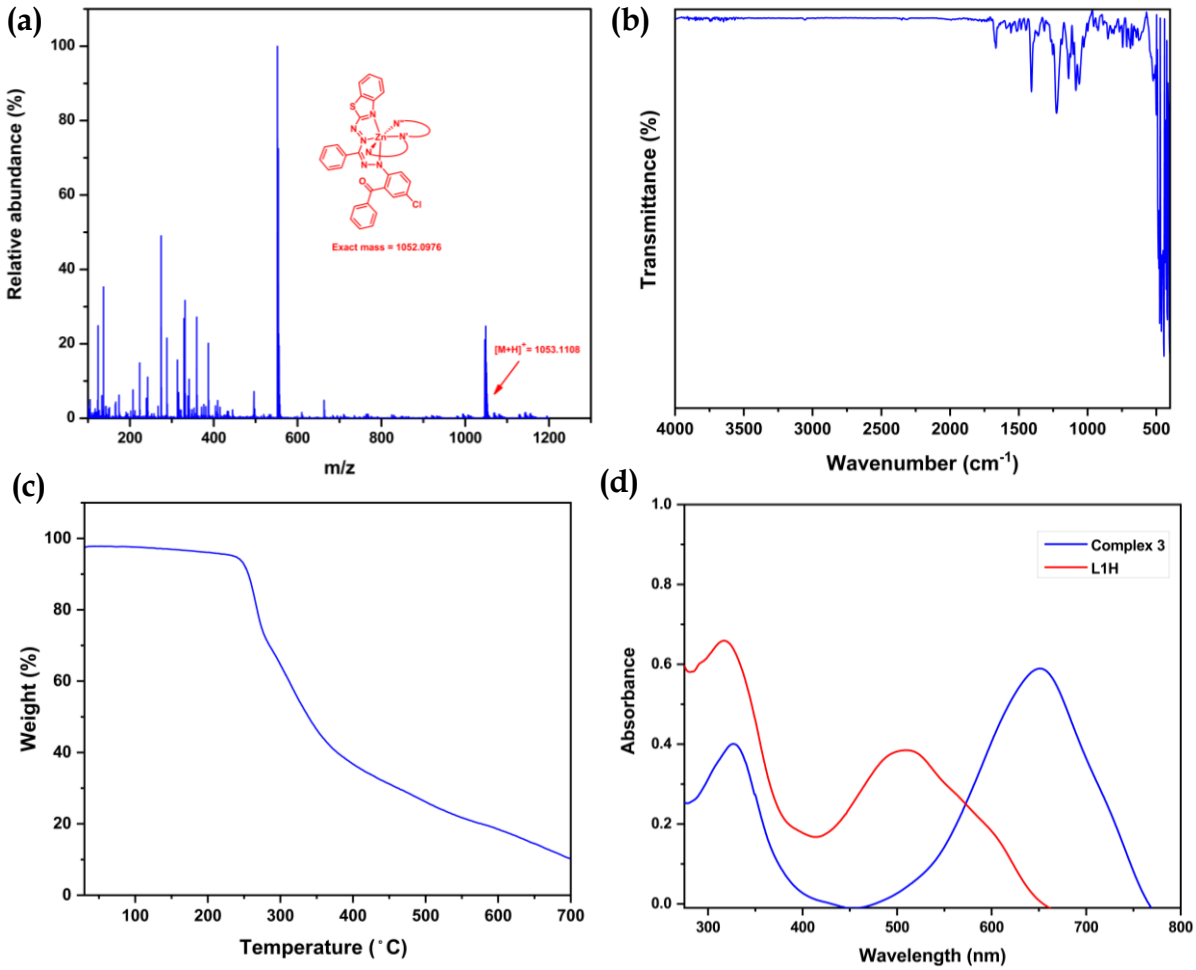


Figure 5.4. (a) HRMS analysis for **3**: Anal. Calcd. for $[M+H]^+$ peak, m/z =1053.1048. Found $[M+H]^+$ peak, m/z = 1053.1108. (b) FTIR spectrum of **3** (c) Thermogravimetric analysis of **3** (d) Absorption spectra of LH and compound **3** in chloroform solution.

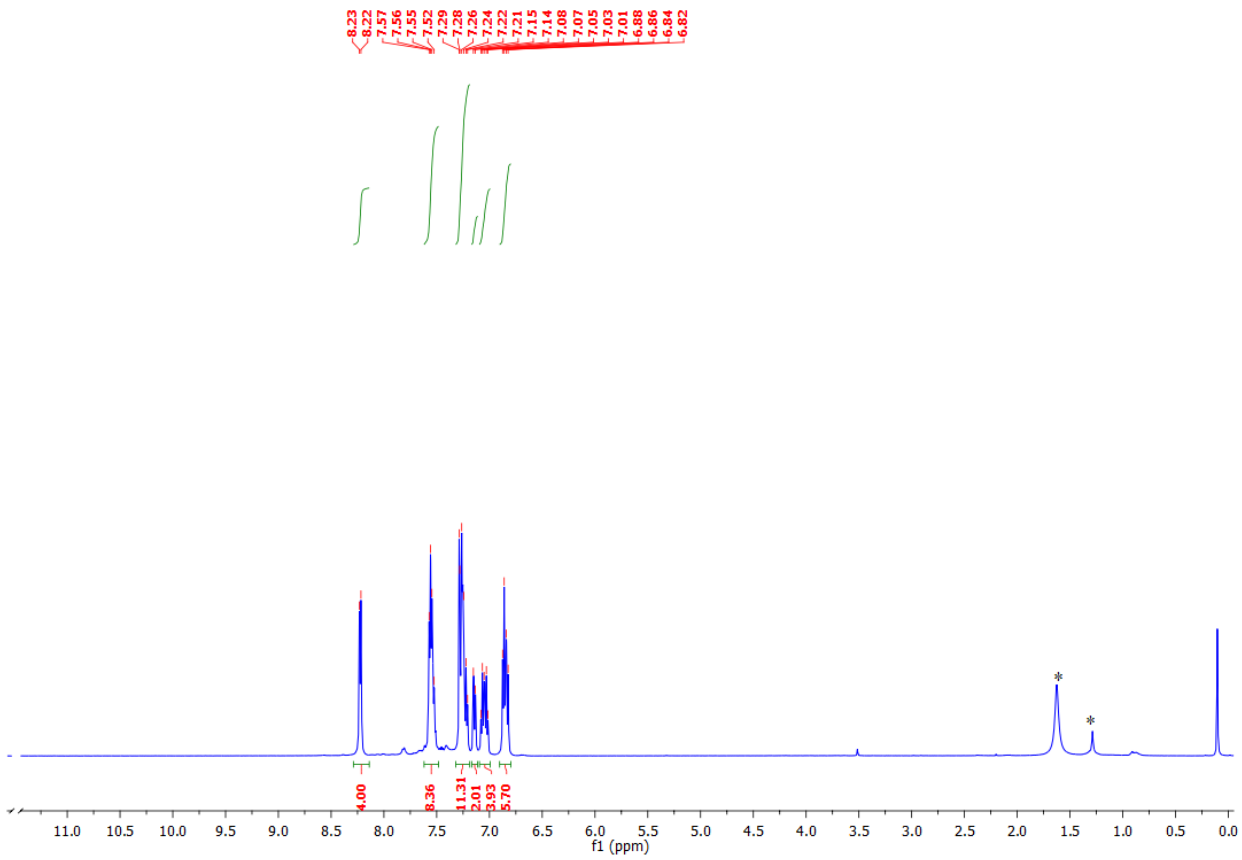


Figure 5.5. ^{1}H NMR (500 MHz, $CDCl_3$) of complex **3**.

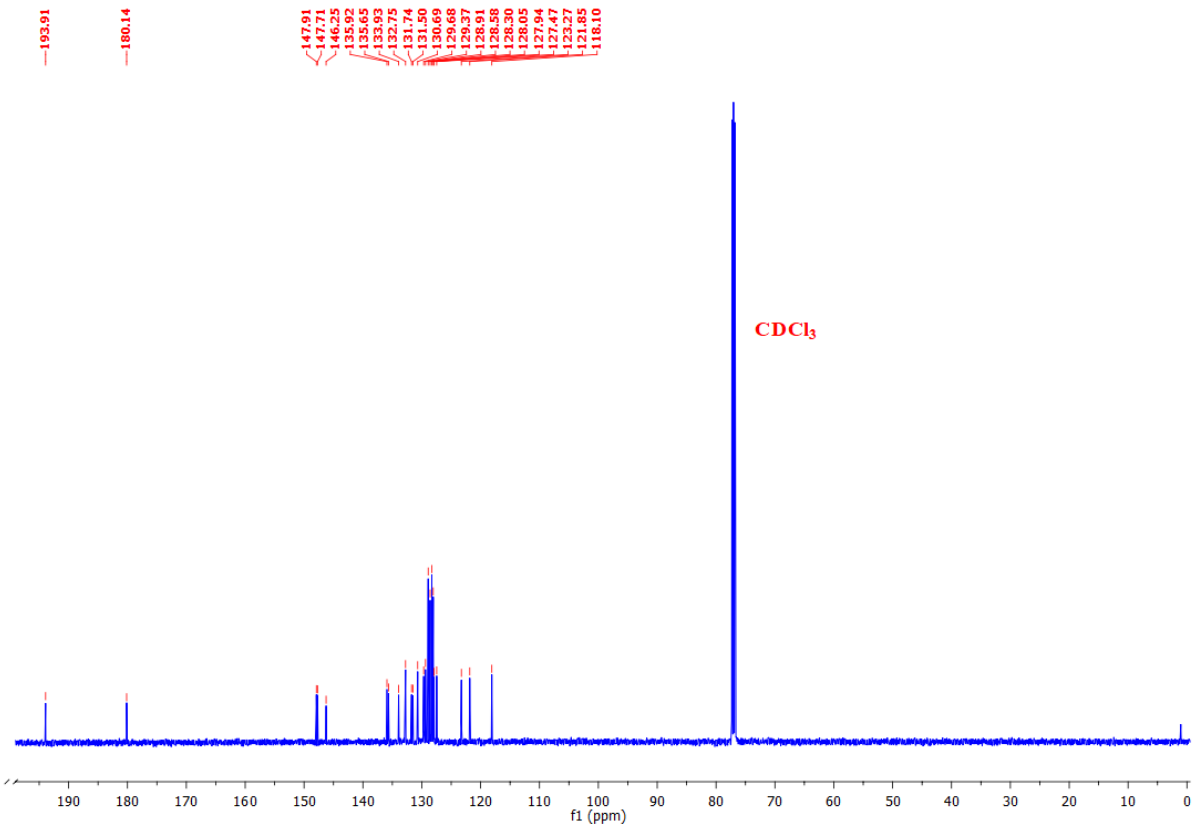
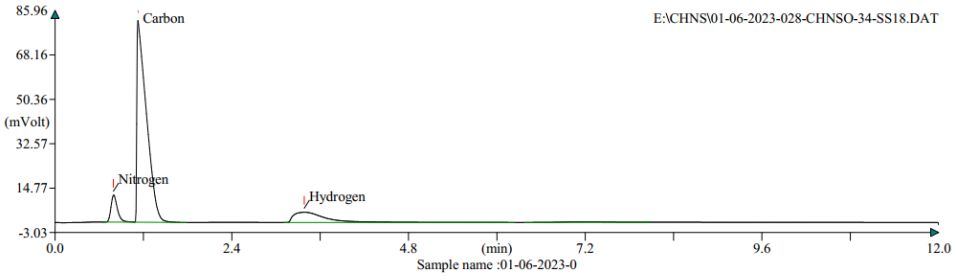


Figure 5.6. ^{13}C NMR (126 MHz, $CDCl_3$) of complex **3**.



Peak Number (#)	Retention Time (min)	Area (.1*uV*sec)	Element %	Component Name
1	0.792	660180	12.895	Nitrogen
2	1.125	7313276	61.724	Carbon
3	3.383	1241559	3.311	Hydrogen

Figure 5.7. Elemental analysis of **3**. Anal. Calcd. (%) for C54H34Cl2N10O2S2Zn: C, 61.46; H, 3.25; N, 13.27. Found: C, 61.72; H, 3.31; N, 12.89.

5.3.2 X-Ray Crystallography

Figure 5.8 displays the perspective view of the molecular structure of complex **3,** which comprises a distinct mononuclear molecular unit. Complex **3** crystallizes in a monoclinic system with the space group P $2_1/n$. The crystallographic and structure refinement data for the **3** are shown in Table 5.2. Complex **3** is neutral, whereby the stability of the electrical charge on the metal center is achieved via the presence of two deprotonated formazan ligands ($L1^-$). The Zn center adopts a distorted octahedral geometry, with the coordination sites consisting of the six nitrogen donor atoms from the two tridentate benzothiazole substituted formazan ligands. Two five-membered rings are formed since Zn is coordinated to one terminal, one non-terminal N atom of the formazan backbone, and one N atom of benzothiazole substituent. The N-N [1.276(2)–1.342(2) Å] and C-N [1.319(2)–1.406(2) Å] bond lengths of formazanate scaffold lay between the single and double bond lengths of the corresponding atoms. While the phenyl substituent is slightly twisted with respect to the plane defined by the N4 atoms of the formazanate backbone, the benzothiazole substituent was determined to be in the plane. Together, these structural metrics point to a substantial electronic delocalization along the N-aryl substituents and formazanate ligand backbone. Despite the fact that nitrogen atoms occupy all of the vertices of the coordination octahedron, the lengths of its Zn–N bonds vary, ranging from 2.089(15) Å to 2.286(16) Å. Table 5.1 summarises the selected bond angles and distances for complex **3**. The dihedral angle between two formazanate coordination planes for **3** is found to be 87.139° (Figure 5.8(c)).

Figure 5.9(a) depicts the unit cell of complex **3**, revealing that it contains four molecules where the zinc atoms are spaced apart by distances of 8.163 Å and 11.096 Å. These molecules engage with one another due to the presence of CH--O, CH--S, and π--π interactions. Additional insight into the supramolecular assembly of compound **3** is displayed in Figure 5.9(b), highlighting the existence of CH--π and CH--Cl interactions.

5.3.3 UV–Vis Spectroscopy

UV-vis absorption spectroscopy was used to analyze the optical characteristics of the free formazan ligand, L1H, and intensely colored bis(formazanate)zinc complex, **3** in a $CHCl_3$ solution in the 200-800 nm wavelength range (Figure 5.4(d)). The free ligand L1H exhibits a strong absorption band in the visible spectrum (507 nm), which is caused by transitions between π- π* inside the formazanate framework. As a result of the interaction with the metal d-orbitals, the complexation of the ligand with Zn(II) in **3** results in shifts to longer wavelengths, from 507 nm to 651 nm, which is consistent with a decrease in π- π* energy. Further, we have compared the UV-Vis spectra of complex **3** ($Zn^{II}L_2$) to the previously reported bis(formazanate) zinc complex ($Zn^{II}L_2$, **2**) based on 3-cyano-1,5-(4-antipyrinyl)formazan (LH) ligand (Figure **5.10(a)**) [Birara, Saini, et al., 2023]. The UV-Vis spectra of complex **3** show a red shift in the λ_{max} value of around 100 nm when compared to the reported [$Zn^{II}L_2$] (**2**) complex. This could be due to the inclusion

of a benzothiazole substituent and the carbonyl unit, which has an electronic impact on complex **3**, indicating that the presence of these substituents greatly influences the optoelectronic characteristics [Buguis et al., 2022b; Turkoglu & Berber, 2016]. Gilroy and co-workers demonstrated that the inclusion of a benzothiazole substituent causes a shift in the absorption band towards lower energy levels in BF_2 formazanates [Buguis et al., 2022b]. The intense absorption bands observed in the range of 550-800 nm for the metal complex can be described as a combination of n → π* and π → π* electronic transitions (Table 5.4). The band observed at λ = [600-650] nm is best represented by the electronic transitions between molecular orbitals, as shown in Figure 5.10(b) with LLCT character.

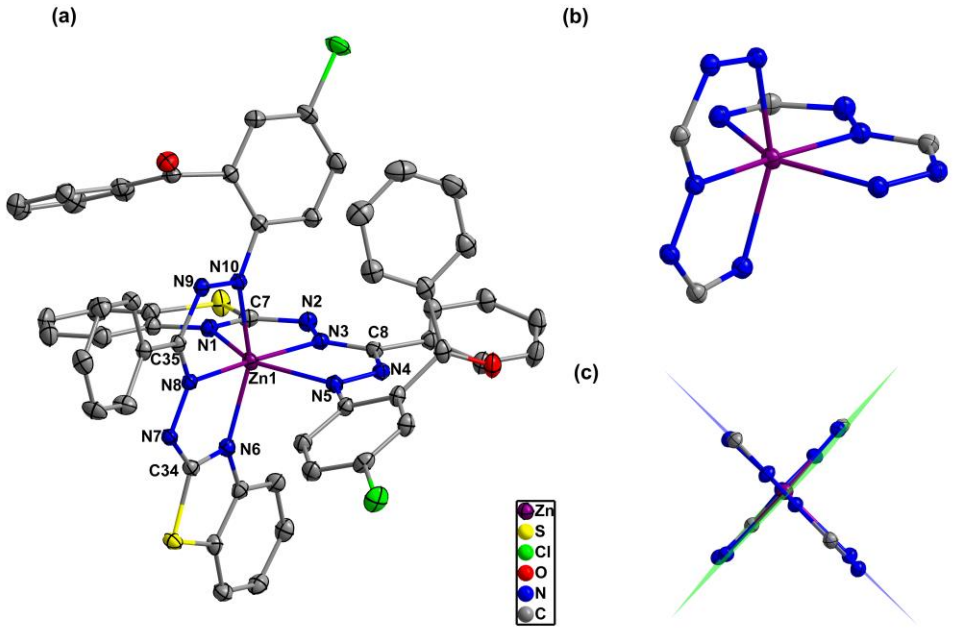
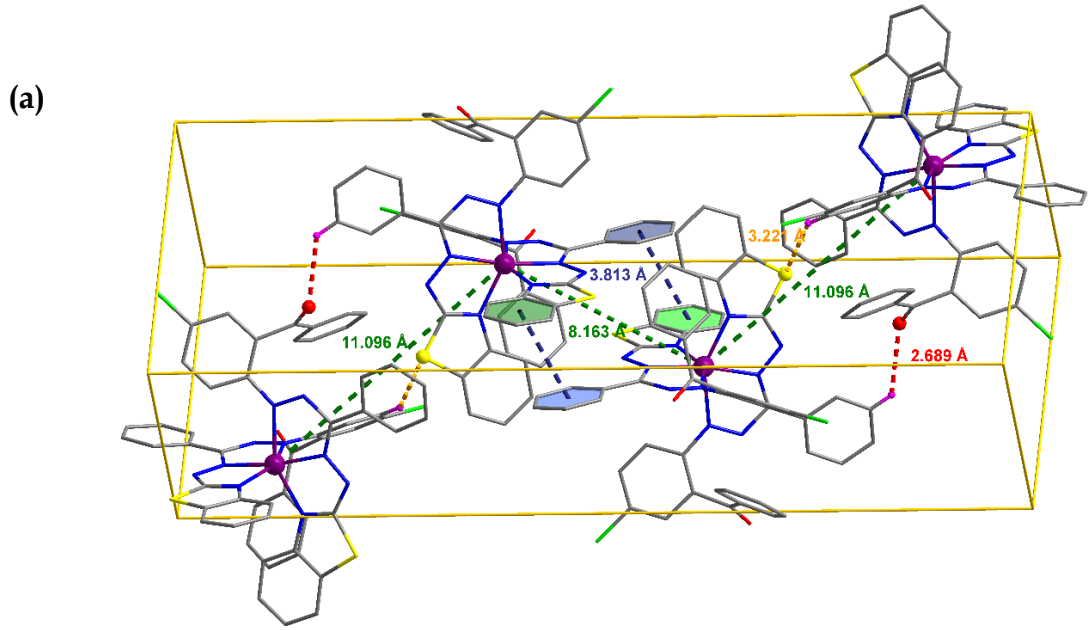


Figure 5.8. (a) Molecular structure of **3** showing 50% probability ellipsoids. (b) Coordination environment around Zn atom (c) The $Zn(NNCNNCN)_2$ core of the structure with the N–Zn–N planes and the dihedral angle.



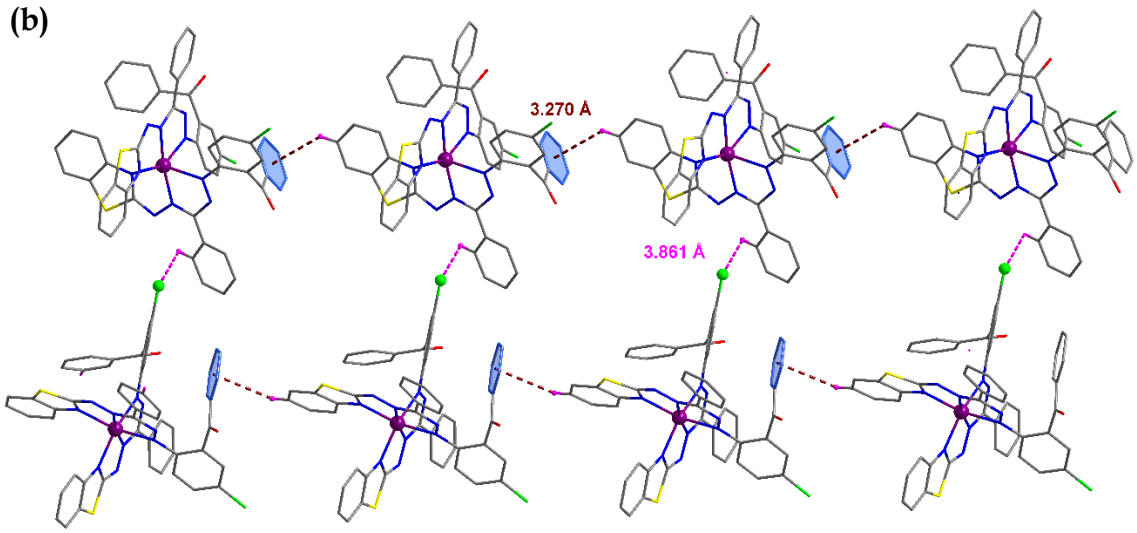


Figure 5.9. (a) Unit cell of complex **3** displaying CH--O, CH--S, and π--π interactions**.** (b) Crystal packing mode in **3** displaying CH--π and CH--Cl interactions.

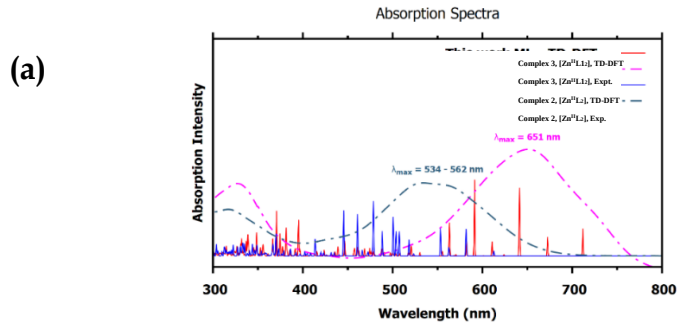
Table 5.1. Selected Bond Angles (deg) and Selected Bond Distances (Å) for **3**.

3			
N2-N3	1.342 (2)	N7-N8	1.342 (2)
N3-C8	1.319 (2)	N8-C35	1.319 (2)
C8-N4	1.406 (2)	C35-N9	1.405 (2)
N4-N5	1.277 (2)	N9-N10	1.276 (2)
Zn1-N1	2.100 (16)	Zn1-N6	2.099 (16)
Zn1-N3	2.094 (15)	Zn1-N8	2.089 (15)
Zn1-N5	2.286 (16)	Zn1-N10	2.239 (15)
N1–Zn1–N3	76.81 (6)	N6–Zn1–N8	76.65 (6)
N3–Zn1–N5	71.94 (6)	N8–Zn1–N10	72.62 (6)
N1–Zn1–N5	148.75 (6)	N3–Zn1–N8	171.26(6)
N6–Zn1–N10	149.25 (6)		

Table 5.2. Crystal data and structure refinement for **3** (CCDC 2356039).

Identification code	**3**
Empirical formula	$C_{54}H_{34}Cl_2N_{10}O_2S_2Zn$
Formula weight	1055.30
Temperature/K	100
Crystal system	monoclinic
Space group	$P2_1/n$
a (Å)	11.2270(4)
b (Å)	31.2653(9)
c (Å)	14.0665(5)
α (°)	90
β (°)	111.5770(10)
γ (°)	90
Volume (Å³)	4591.6(3)
Z	4

ρ_{calc}g.cm^{-3}	1.527
μ, mm^{-1}	0.800
F(000)	2160.0
Crystal size (mm^3)	0.26 × 0.23 × 0.22
Radiation	MoKα (λ = 0.71073)
2Θ range for data collection (°)	4.114 to 56.582
Index ranges	-14 ≤ h ≤ 14, -38 ≤ k ≤ 41, -18 ≤ l ≤ 18
Reflections collected	78484
Independent reflections	11378 [R_{int} = 0.0434, R_{sigma} = 0.0275]
Data/restraints/parameters	11378/0/640
Goodness-of-fit on F^2	1.050
Final R indexes [I>=2σ (I)]	R_1 = 0.0373, wR_2 = 0.0887
Final R indexes [all data]	R_1 = 0.0459, wR_2 = 0.0925
Largest diff. peak/hole (e Å^{-3})	0.67/-0.46



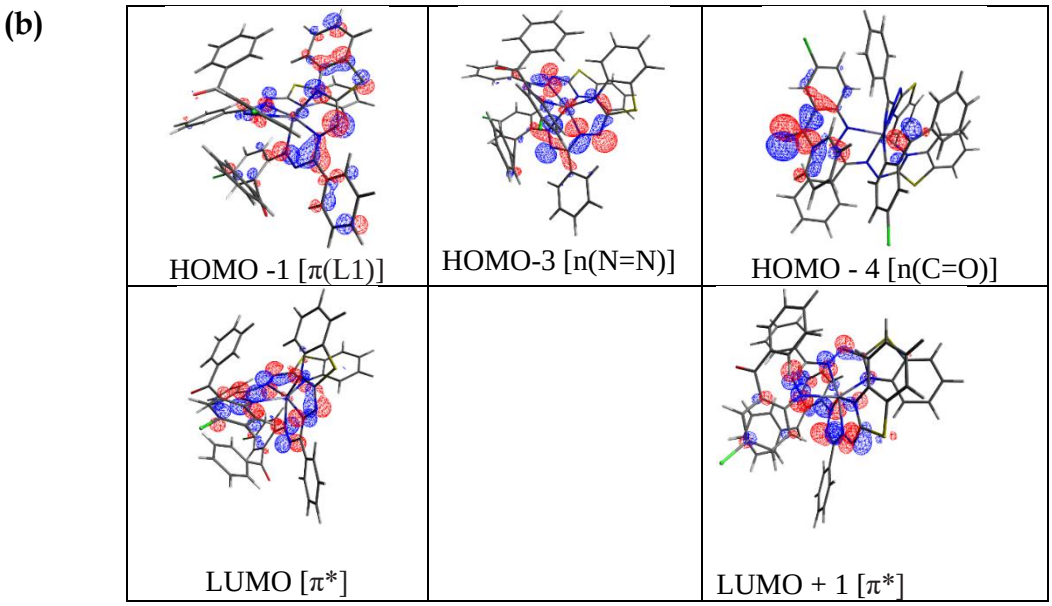


Figure 5.10. (a) Experimental and Computed absorption spectra of complex **3** (This work), and complex **2** [Birara, Saini, et al., 2023] (Previous work) in $CHCl_3$ solution. (b) The molecular orbital representations of electronic transition that appear at the wavelength range from 600–650 nm (oscillator strength = 0.37-0.42) of TD-DFT computed absorption spectrum of complex **3** in $CHCl_3$ solvent. A contour value of 0.04 au is used to generate the plots.

5.3.4 Resistive Memory Device Studies

Complex **3** was investigated as a switching active layer in Ag/[$Zn^{II}L1_2$] (**3**)/FTO RRAM devices where Ag and fluorine-doped tin oxide (FTO) were used as the top electrode (TE) and bottom electrode (BE), respectively. The metal-insulator-metal (MIM) structure of the fabricated RRAM devices is shown in Figure 5.11(a). To investigate the switching behavior, linear voltage dual sweep from 0 → 2 V → 0 → -2 V → 0 V was applied across TE and BE. The corresponding I-V characteristics are shown in Figure 5.11(b**)**. Initially, the results show that the device was in a high resistance state (HRS), which indicates the filament is not present in the switching layer. When positive voltage was applied to the device, a sharp change in current at ~ 0.9 V (V_{SET}) was observed, and the device shifted to the low resistance state (LRS). Now, the negative voltage dual sweep was applied across the TE and BE, and the device became RESET at -0.75 V (V_{RESET}), and the resulting device reached from LRS to HRS. The device shows excellent switching behavior with I_{ON}/I_{OFF} around ~10^3 and very low V_{SET}/V_{RESET} (0.9 V/ -0.75 V) voltages.

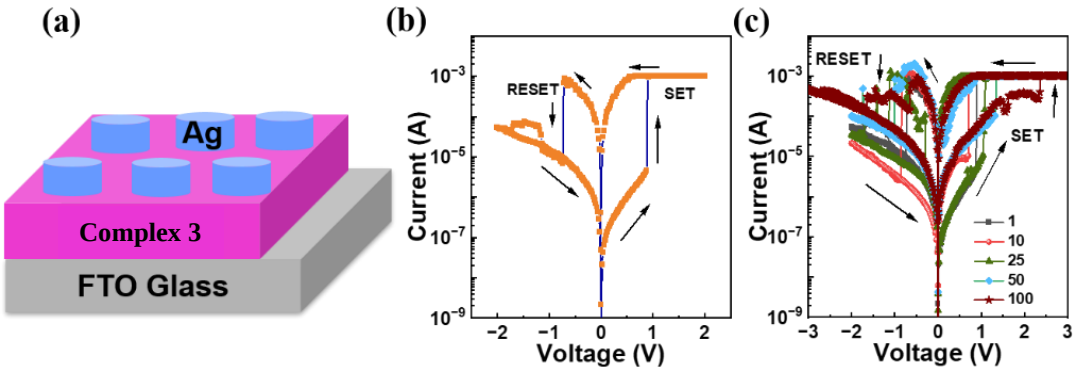


Figure 5.11. (a) Device structure, (b) I-V characteristics, and (c) multiple cycles I-V characteristics of Ag/$Zn^{II}L1_2$/FTO RRAM device.

Now, the repeatability of the device was checked by applying 100 consecutive dual sweep voltage cycles, and the corresponding I-V characteristics of multiple cycles are plotted in Figure 5.11 (c). The results indicate that the device shows decent resistive switching even after 100 times continuously SET and RESET the device.

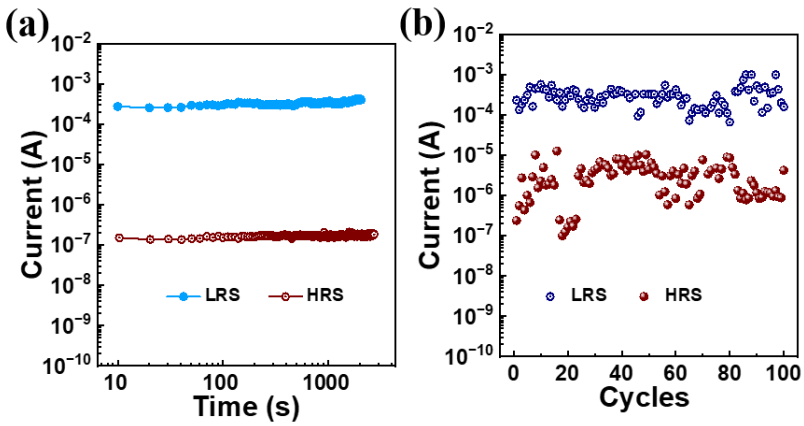


Figure 5.12. (a) Retention time characteristics and (b) endurance characteristics.

The non-volatile memory behavior of RRAM devices was investigated by plotting the retention time characteristics for more than 2000 seconds, as shown in Figure 5.12 (a). It can be observed that I_{ON}/I_{OFF} (~10^3) and switching states (LRS/HRS) are maintained until the external voltage sweep is applied across the TE and BE of the device to change the state from LRS to HRS or vice versa. The endurance characteristics of the Ag/$Zn^{II}L1_2$ (**3**)/FTO RRAM device for 100 consecutive cycles are shown in Figure 5.12 (b). Both LRS and HRS currents are plotted at the read voltage of 0.2 V. The acceptable variation in LRS and HRS was observed even after the 100

consecutive I-V cycles, which indicates the decent resistive switching behavior of the device. The cycle-to-cycle variability of fabricated RRAM devices was checked by Weibull distribution of LRS and HRS as shown in Figure 5.13(a&b) respectively, and the cumulative distribution of SET and RESET voltages are shown in Figure 5.13(c&d) respectively. The LRS and HRS current scale values are found to be 3.5E-4 A and 3.47E-6 A, respectively. The average values of V_{SET} and V_{RESET} of 100 consecutive *I-V* DC voltage sweep cycles are 1.2 V and -1.27 V, respectively. To check the consistency of the devices, the device-to-device variation of five randomly chosen devices on the same sample is shown in Figure 5.13(e). The average value of SET and RESET voltages of 20 cycles for each device with standard deviation show the reliability of the device. The acceptable variation in LRS and HRS was observed, and the resistive switching behavior can be seen clearly at each cycle of the device. Resistive switching analysis results show that the fabricated Ag/$Zn^{II}L1_2$ (**3**)/FTO RRAM devices exhibit excellent switching performance with very low V_{SET} and V_{RESET} (~0.9 V and -0.75 V) voltages, excellent I_{ON}/I_{OFF} (~10^3) and retention time of more than 2000 seconds. Moreover, Ag/$Zn^{II}L1_2$ (**3**)/FTO RRAM devices can be a suitable choice for low-power switching operation memory applications.

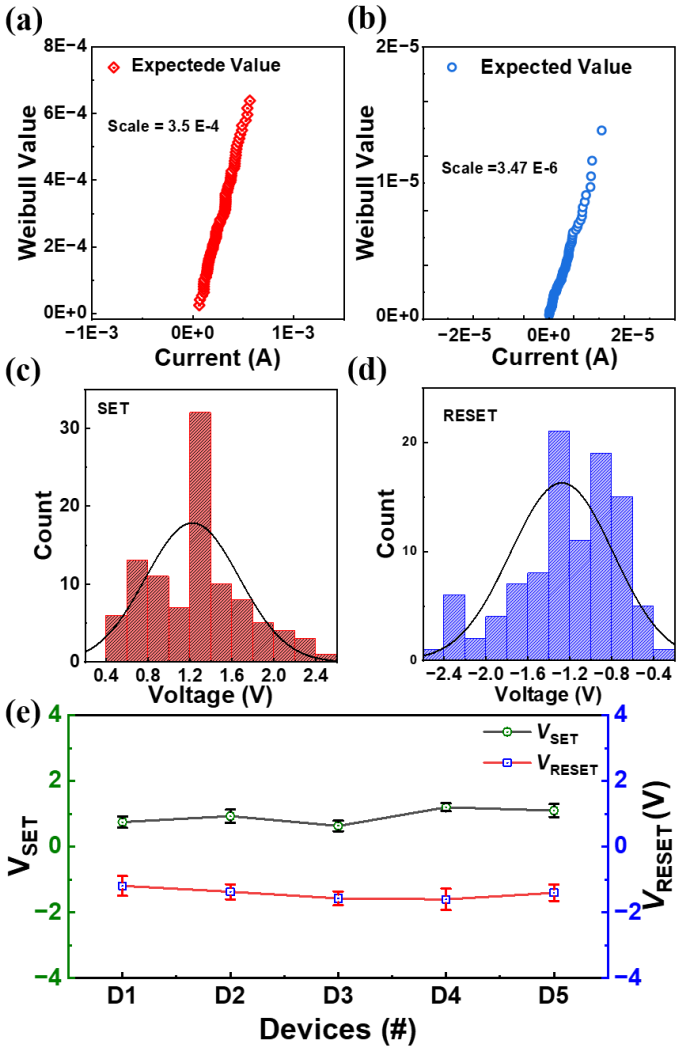


Figure 5.13. (a&b) Weibull distribution of LRS and HRS currents, (c&d) Cumulative distribution of SET/RESET voltages of 100 *I-V* cycles. (e) the average value of SET and RESET voltages of five devices to check the device-to-device variability

5.3.5 Cyclic Voltammetry, DFT Studies, and Proposed Memory Mechanism

In earlier studies, it has been shown that the formazanate ligands in the zinc complexes possess the ability to undergo stepwise and reversible reduction, resulting in the formation of the

corresponding radical anions (L_2Zn^{-}) and diradical dianions (L_2Zn^{2-}). Furthermore, it was discovered that some zinc complexes exhibited further reductions, which may be attributed to the two-electron reduction of each formazanate ligand, resulting in the formation of $L_2Zn^{1-/2-/3-/4-}$ species. The redox chemistry of the bis(formazanate)zinc complex, **3** has been investigated by using cyclic voltammetry in DMF with a $[Bu_4N][PF_6]$ electrolyte (Figure 5.14). Compound **3** exhibits a quasi-reversible redox wave at a potential of -0.87 V (ΔE = 70 mV) and a second, less reversible reduction at -1.36 V (ΔE = 60 mV) with all potentials referenced to Ag/AgCl. The first reduction occurring at a potential of -0.87 V is most likely responsible for the formation of the radical anion $3^{\bullet-}$, whereby one electron is transferred to the formazanate ligand. Upon further sweeping into a more negative potential, a second reduction occurs, resulting in the formation of the two-electron-reduced complex 3^{2-}. The quasi-reversible wave appearing at +0.19 V (ΔE = 110 mV) vs Ag/AgCl may be attributed to the oxidation of the ligand. According to the equations $E_{HOMO} = -[E_{onset}(oxidation) + 4.8 – E_{FOC}]$ (eV) and $E_{LUMO} = -[E_{onset}(reduction) + 4.8 – E_{FOC}]$ (eV) where E_{FOC}[Wang et al., 2023] means the external standard potential of the ferrocene/ferrocenium couple, the HOMO and LUMO energy levels of the Zn(II) complex are calculated to be -4.6 eV and -4.12 eV, respectively which indicates that complex **3** exhibits a high degree of conjugation [Perepichka & Bryce, 2005].

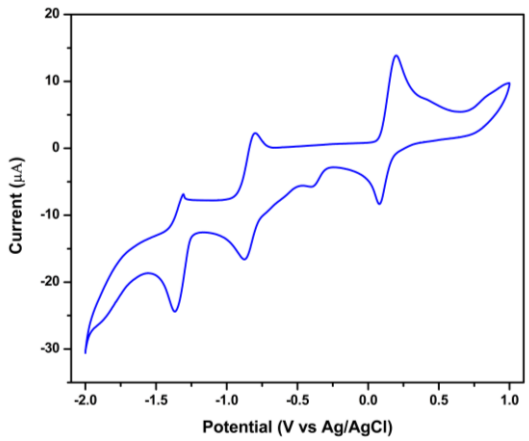


Figure 5.14. Cyclic voltammogram of **3** (1.5 mM in DMF solution, 0.1 M $[Bu_4N][PF_6]$) recorded at 10 mVs^{-1} acquired using a Pt-wire counter electrode, glassy carbon working electrode, and Ag/AgCl (3.0 M KCl) reference electrode.

However, the results obtained from electrochemical calculations are slightly different from those obtained through the Density Functional Theory (DFT). The BP86+D3BJ/def2-TZVPP+SDD computed the Highest Occupied Molecular Orbital (HOMO) and Lowest Unoccupied Molecular Orbital energy of the complex are found to be -5.14 and -4.06 eV, respectively, in a vacuum. As reported in the previous literature, this variance may be attributed to the influence of the solid-state conjugation network effect and the interaction of solvent molecules, affecting the calculated energy level values from the experimental data [Stachowiak et al., 2021]. The DFT computed frontier molecular orbitals of the closed-shell complex are shown in Figure 5.16 (a). The FMOs energy corresponding to uncoordinated benzothiazole-substituted formazan ligand molecule (L1H) is found to be HOMO = -5.30 and LUMO = -4.02 eV from DFT computations (Figure 5.15).

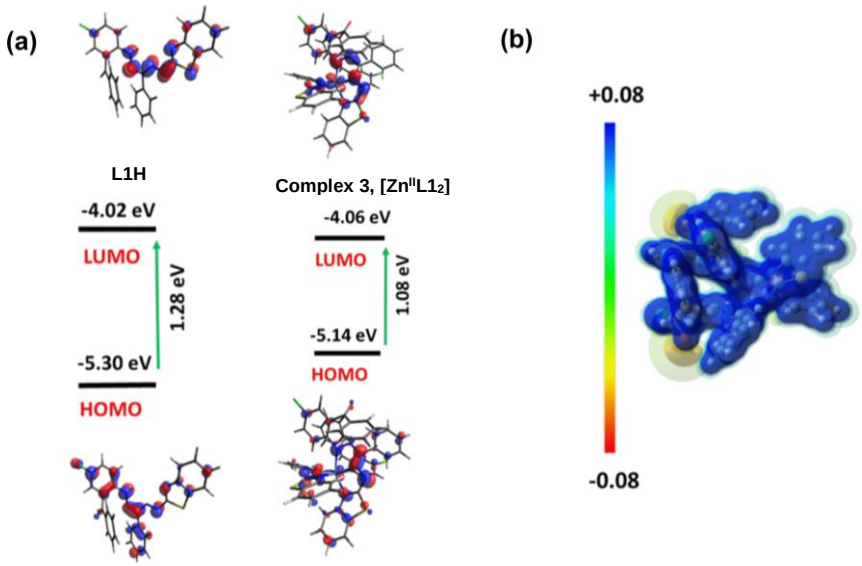


Figure 5.15. (a) BP86 computed frontier molecular orbitals of the Zn-metal complex **3** and uncoordinated benzothiazole-substituted formazan ligand (L1H) are plotted with an isosurface value of 0.04 au. (b) The molecular electrostatic potential surface (isovalue: 0.025, 0.05, 0.08) of complex **3**, the positive and negative ESP regions are represented by blue and red colors, respectively.

As inferred from molecular orbital analysis of the complex, the FMOs of the formazanate Zn complex are primarily ligand-based and highly delocalized over the ligand backbone. As observed in our previous study [Birara, Saini, et al., 2023], the metal ion (Zn^{II}) acts as a dopant and reduces the HOMO-LUMO energy gap by modifying the FMOs energy values of the substituted/unsubstituted formazan ligand. The energy levels of FMOs, along with the work function (φ) of two conducting electrodes (Ag and FTO), are briefed in Figure 5.16 (a). The energy barrier (0.34 eV) between the LUMO level and φ of FTO is low, as compared to the barrier value (0.95 eV) between the φ value of Ag and HOMO level of the complex. Unlike the previously reported complex (Figure 5.16 (b)), where the hole injection initiates the device [Birara, Saini, et al., 2023], in the present complex, the electron injection from FTO to LUMO of the metal complex initiates the device when a positive voltage is applied. The electron injection in a conjugated complex is generally unusual, as it is already electron-rich. However, installing an electron donor-acceptor group can facilitate the electron injection process by stabilizing the LUMO and reducing the HOMO-LUMO energy gap. It is demonstrated in the literature that the inclusion of a benzothiazole ring greatly enhances the stability of the LUMO level [Buguis et al., 2022b]. As inferred from the NBO analysis, the large estimated LP(*2p*)S→ π*(C-N) [~29 kcal/mol] and LP(*2p*)S→ π*(C-C) [~17 kcal/mol] second-order NBO-NBO* interaction energy values (Table 5.3) are consistent with the strong donor-acceptor interaction. The enhancement in the donor-acceptor interaction is also reflected in the UV-visible absorption spectra of the benzothiazole-substituted formazan metal complex **3**, as the λ_{max} of the complex **3** appears nearly 100 nm redshifted than that of previously reported bis(formazanate) Zinc complex based on 3-cyano substituted formazan (as shown in Figure 5.10 (a)).

Additionally, to identify the conduction mechanism in the Ag/$Zn^{II}L1_2$ (**3**)/FTO RRAM device, a double log (I-V) graph of the device is plotted for both (positive voltage) SET and (absolute negative voltage) RESET state as depicted in Figure 5.16 (a), and 5.16 (b). The conduction mechanism can be easily identified by the slope values of the linear fitting curve of double log (I-V) plots [Saini, Dwivedi, et al., 2023b; Saini, Lodhi, et al., 2023b]. Here, the slope value (~1) shows that the current linearly increases with the increasing applied voltage, and the device is in the ohmic or linear conduction region ($I \propto V$). The slope value (~2) indicates the space charge limited conduction (SCLC). In Ag/$Zn^{II}L1_2$ (**3**)/FTO RRAM device at lower voltage side ohmic conduction and at higher voltage side SCLC mechanism was observed.

Table 5.3. Second-order perturbation energy E_2 (eV), off-diagonal Fock matrix elements *F(i,j)*, and acceptor – donor energy values $(E_j - E_i)$ (a.u.) of selected donor-acceptor NBO-NBO* interactions in metal-complex **3**, as computed at BP86+D3/TZVPP+SDD method. $E_2 > 1.0$ kcal/mol are tabulated here

Donor NBO (i)	Acceptor NBO(j)	E_2 (kcal/mol)	$E_j - E_i$ (au)	F(i,j)
Ligand-to-Metal				
LP(1)N	LP*(1)Zn	29.57 - 34.77	0.36 - 0.39	0.094 - 0.101
Ligand-to-Ligand				
LP(2)S	π*(N-C)	29.02	0.17	0.062
LP(2)S	π*(C-C)	17.26	0.20	0.053
LP(3)Cl	π*(C-C)	14.35	0.25	0.054
LP(1)N	π*(N-N)	1.64	0.24	0.018
LP(1)N	π*(C-C)	1.43	0.33	0.019
LP(1)N	π*(O-C)	5.39	0.30	0.036
LP(1)N	π*(N-C)	1.38	0.24	0.016
π(O-C)	π*(C-C)	4.76	0.33	0.035
π(N-N)	C(LP*)	41.10, 28.03	0.19, 0.22	0.079,0.069
π(N-N)	π*(N-N)	1.36, 19.95	0.23, 0.26	0.016, 0.064
π(N-N)	π*(C-C)	10.28	0.33	0.052
π(N-C)	π*(N-N)	8.72	0.22	0.039
π(N-C)	π*(C-C)	17.98	0.28	0.063
π(C-C)	π*(O-C)	17.12,4.09	0.21	0.053
π(C-C)	π*(N-N)	16.49	0.15	0.010
π(C-C)	π*(C-C)	11.51 – 19.07	0.24 – 0.21	0.047-0.056
π(C-C)	π*(N-C)	9.57	0.19	0.038
π(C-C)	LP*C18	65.90	0.09	0.069

Table 5.4: Calculated TD-DFT electronic transition wavelength (nm), oscillator strength (f_{osc}), major compositions in terms MO contributions, and electronic transition character for complex **3** ($Zn^{II}L_2$)

S. no.	Wavelength (nm)	f_{osc}	Major composition	Transition Character
Complex 1				
1.	712	0.15	(HOMO-2) → LUMO	n → π*
2.	673	0.10	(HOMO-2) → LUMO	n → π*
3.	641	0.37	(HOMO-1) + (HOMO-3) → LUMO	n + π (L) → π*
4.	611	0.08	(HOMO-2) → LUMO+1	n → π*
5.	591	0.42	(HOMO-1) + (HOMO-3) → LUMO (HOMO-1) + (HOMO-4) → LUMO+1	n + π (L) → π* n → π*
6.	582	0.18	(HOMO-3) → (LUMO+1)	n → π*
7.	555	0.03	(HOMO-7) → LUMO + (LUMO+1)	S(LP)+π → π*
8.	530	0.02	(HOMO-6) → LUMO + (LUMO+1)	S(LP)+π → π*

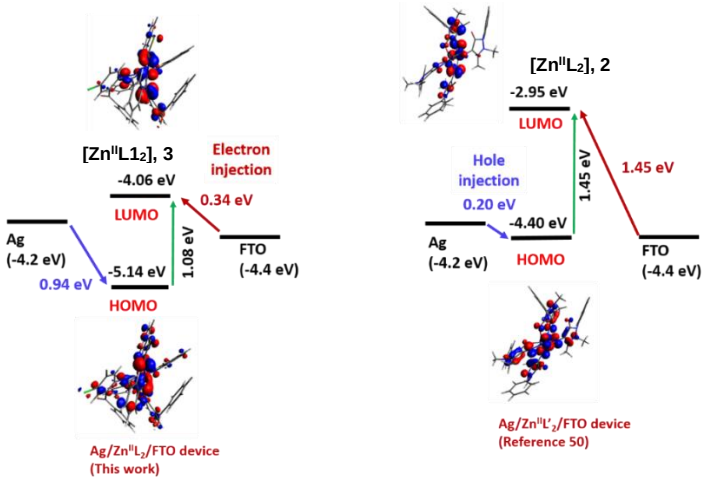


Figure 5.16. Schematic diagram of two memory devices a) Ag/Zn^{II}L1$_2$/FTO) [L1=1-(benzothiazol-2-yl)-5-(2-benzoyl-4-chlorophenyl)-3-phenylformazan)] [This work] b) Ag/Zn^{II}L$_2$/FTO) [L=3-cyano-1,5-(4-antipyrinyl)formazan] [Previous work] and their plausible operating mechanism during a positive voltage bias.

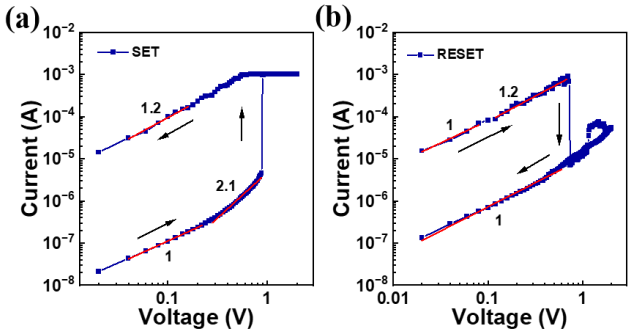


Figure 5.17. Double log (I-V) characteristics of Ag/Zn^{II}L1$_2$ (**3**)/FTO RRAM device (a) SET, and (b) RESET.

5.4 Conclusion

In summary, an electroactive [Zn^{II}L1$_2$] (**3**) complex based on redox-active formazanate ligand, L1H, has been successfully synthesized and thoroughly characterized using various analytical techniques. The determination of the crystal structure of complex **3** has been established by the use of single-crystal X-ray crystallographic measurement. Complex **3** exhibited the distorted octahedral geometry by the formation of four five-membered chelate rings, but no six-membered metallacycle was observed. The cyclic voltammetry (CV) result indicates the occurrence of reversible redox chemistry involving the formazanate ligand in complex **3**. These findings demonstrate the formation of the redox series L1$_2$Zn$^{0/1-/2-}$, as well as the possibility of oxidation of the ligand. Furthermore, we have fabricated an RRAM device utilizing [Zn^{II}L1$_2$] (**3**) complex as an active switching material with Ag and FTO taken as TE and BE, respectively. The fabricated RRAM devices displayed excellent resistive switching characteristics such as a high I_{ON}/I_{OFF} (~10^3), very low V_{SET} and V_{RESET} with decent endurance stability (100 cycles), and a prolonged retention time of more than 2000 seconds. This work reveals that using benzothiazole-substitution in ligand enhances the donor-acceptor interaction and thus lowers the LUMO energy of the metal complex, resulting in a low barrier electron injection from the FTO electrode to the LUMO of the complex **3**. Further, the π-conjugated backbone of the ligand supports the hole transportation in the active layer. Thus, by judiciously modifying the structure of the formazan backbone, it is possible to determine how substituents affect the optical and electrochemical properties of the backbone, which can further be used to enhance the performance of memory devices.